ACS Catalysis

Research Article

pubs.acs.org/acscatalysis

Easy Accommodation of Different Oxidation States in Iridium Oxide Nanoparticles with Different Hydration Degree as Water Oxidation Electrocatalysts

Alessandro Minguzzi,[*,†,‡] Cristina Locatelli,[†,‡] Ottavio Lugaresi,[†] Elisabetta Achilli,[‡] Giuseppe Cappelletti,[†] Marco Scavini,[†,‡,∥] Mauro Coduri,[†,⊥] Paolo Masala,[†] Benedetta Sacchi,[†] Alberto Vertova,[†,‡,∥] Paolo Ghigna,[§] and Sandra Rondinini[†,‡,∥]

[†]Dipartimento di Chimica, Università degli Studi di Milano, Via C. Golgi 19, I-20133 Milano, Italy

[‡]Consorzio Interuniversitario Nazionale per la Scienza e Tecnologia dei Materiali − INSTM, Milano Unit, Via Golgi 19, 20133 Milano, Italy

[§]Dipartimento di Chimica, Università di Pavia, Via Taramelli 18, 27100 Pavia, Italy

[∥]CNR, Istituto di Scienze e Tecnologie Molecolari - ISTM, Via Golgi 19, 20133 Milano, Italy

[⊥]CNR, Istituto per l'Energia e le Interfasi, - IENI, C.so Promessi Sposi 29, 23900 Lecco, Italy

Supporting Information

ABSTRACT: In this paper, we present a comprehensive study on low hydration Ir/IrO_2 electrodes, made of an Ir core and an IrO_2 shell, that are designed and synthesized with an innovative, green approach, in order to have a higher surface/bulk ratio of Ir−O active centers. Three materials with different hydration degrees have been deeply investigated in terms of structure and microstructure by means of transmission electron microscopy (TEM) and synchrotron radiation techniques such as high-resolution (HR) and pair distribution function (PDF) quality X-ray powder diffraction (XRPD), X-ray absorption spectroscopy (XAS), and for what concerns their electrochemical properties by means of cyclic voltammetry and steady-state *I*/*E* curves. The activity of these materials is compared and discussed in the light of our most recent results on hydrous IrO_x. The main conclusion of this study is that the Ir core is noninteracting with the IrO_x shell, the latter being able to easily accommodate Ir in different oxidation states, as previously suggested for the hydrated form, thus explaining the activity as electrocatalysts. In addition, in operando XAS experiments assessed that the catalytic cycle involves Ir(III) and (V), as previously established for the highly hydrated IrO_x material.

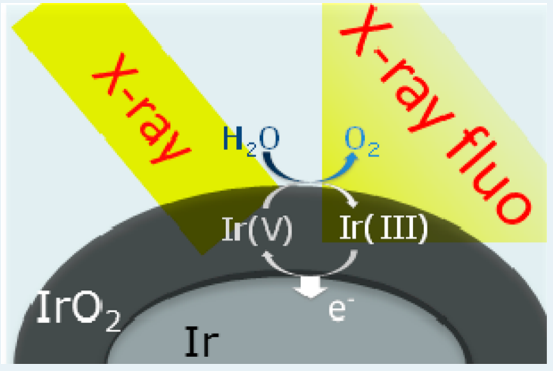

KEYWORDS: *EXAFS, XANES, in operando, HR-XRPD, PDF, water electrolysis, reorganization energy, catalytic cycle*

1. INTRODUCTION

Iridium oxide has undoubtedly been one of the most studied electrocatalysts for water oxidation, after the seminal works on dimensionally stable anodes (DSA anodes), in which the oxidic material is prepared by direct thermal decomposition of relevant precursors.[1] In the last two decades, the main effort was devoted at dispersing the expensive iridium oxide in a stable, low-cost matrix,[2−5] particularly for use in acidic polymer electrolyte water electrolysis. In the most recent years, IrO_2 was considered a promising catalyst in one of the most efficient combinations of photoconverter/catalyst for sunlight-driven hydrogen production, as in ref 6, where IrO_2 colloidal nanoparticles are deposited onto hematite photoanodes to attain 3 mA cm^{-2} at 1.23 V (RHE). However, the activity of IrO_2 as a photoelectrocatalyst is controversial, because some authors demonstrated that, under illumination, it may show lesser activity than materials usually considered worse electrocatalysts (e.g., Pt)[7] or that it can lower the steady-state photocurrent at the highest potentials.[8] Nonetheless, IrO_2 remains the reference material for the oxygen evolution reaction (OER), especially in an acidic environment, due to its high turnover frequency, that was recently compared to other materials by means of dynamic potential/pH diagrams (DPPDs).[9] This is supported by the wide use of IrO_2-based anodes in industrial processes.[10]

Quite recently, new insights on the role of Ir active sites in OER were obtained by some of the present authors by means of X-ray absorption spectroscopy (XAS), allowing the direct observation of more than one Ir speciation during oxygen evolution: the values of III and V to the oxidation states of Ir

Received: March 19, 2015
Revised: July 22, 2015
Published: July 23, 2015

DOI: 10.1021/acscatal.5b01281
ACS Catal. 2015, 5, 5104−5115

active centers during the catalytic cycle were assessed.[11] To this aim, a highly hydrated form of the oxide (electrodeposited iridium oxide films, EIROF), in which all the Ir centers are known to be addressable by the application of external bias, was used in order to be able to work with a bulk techniques like XAS.

EIROF, being a hydrous, amorphous catalyst,[12] is attracting increasing interest because of the possibility of isomorphous layers with high defectivity of each site and, in turn, expected higher activity and a more optimal usage of Ir active sites with respect to crystalline materials. Even though it might not represent the optimal form of IrO_x due to its poor stability,[13] it was shown that hydrous materials show a higher activity when coupled to a semiconductor in a photoelectrochemical cell because of the formation of an adaptive junction.[14]

In the present work, the preparation of different iridium oxide-based materials with different hydration degrees is reported, aiming at finely comparing their features in terms of structure, microstructure, and electrochemical properties. We also aim to either confirm or exclude the existence of an OER catalytic cycle that includes different oxidation states of Ir and to study any possible modification of the Ir chemical environment during the catalytic cycle. This is supported by a detailed morphological, structural, and microstructural study, by means of transmission electron microscopy (TEM), high-resolution (HR) and pair distribution function (PDF) quality X-ray powder diffraction (XRPD). In situ extended X-ray absorption fine structure (EXAFS), X-ray absorption near edge structure (XANES) have been also employed for studying the local chemical environment and electronic structure of Ir under working conditions; PDF analysis allows determining the real space distribution of interatomic distances up to the tens of nanometer scale,[15−17] and supplies important complementary information to EXAFS.

For in situ XAS, high penetration X-rays require a high surface area material to allow the study of surface phenomena, and a material with a high surface/bulk ratio of Ir−O sites is required. Unfortunately, this condition is hardly attainable when a calcination step has to be introduced in the synthetic step to yield low-hydration powders. To this aim, we synthesized Ir/IrO_x composites in which a stable Ir metal core limits the percentage of nonsurface Ir−O sites. We will show that this approach is effective and that the composite Ir/IrO_x materials show good response and stability, at least for the time-length of the experiments considered in the present work.

For the preparation of Ir-core particles, we introduced a synthetic way that exploits a facile synthesis of IrO_x highly hydrated 2 nm nanoparticles[18,19] by introducing an osmosis purification step and then a calcination step where the production of Ir nanoparticles from the Ir(III) precursor occurs concomitantly with the purification step by means of the dialysis membrane, which contains glycerol, a reducing agent. This method can be safely classified among similar ones using alcohols (likely from vegetal extracts) as reducing agents for the preparation of "green" nanoparticles.[20] The electrochemical properties of these materials were investigated by cyclic voltammetry (CV) and analysis of I/E steady-state curves.

Thanks to this approach, the low-hydration materials here considered represent optimal substrates for in operando XAS, the latter leading to the direct observation of the Ir catalytic cycle and to the analysis of the relevant fine structure of the active sites during the OER.

To the authors' best knowledge, the evidence shown here is the first example of in operando XAS on low-hydration electrode materials capable of evidencing a charge-transfer reaction mechanism.

2. EXPERIMENTAL SECTION

2.1. Electrodes and Standards. IrO_x nanoparticles (NPs) were prepared starting with a 17 mM aqueous $IrCl_3 \cdot 3H_2O$ (Alfa Aesar) solution adjusted to pH 13 with aqueous 1 M NaOH and then heated at 90 °C for 20 min under stirring, and immediately cooled in an ice-bath. As reported in ref 19, a blue suspension is thus obtained, which was then purified (and partially reduced as discussed below) by dialysis in a glycerol-containing SpectrumLabs Spectra/Por 4 Basic cellulose membrane. Before purification, an aliquot of the blue suspension was used to prepare the el_IrO_xNPs electrode by immersion of a carbon electrode in the suspension and applying a constant potential of 1.8 V versus a Pt lamina, operating as counter electrode, for 600 s. The support is a custom-made carbon disposable electrode (DRP−P-C11XX, Dropsens) that includes a Ag track for the external electrical connection, properly insulated to avoid any Ag leak into the electrolyte solution. The powder was finally dried at 80 °C to obtain powders P1 and finally calcined. Powder 2 (P2) is the result of calcination of P1 at 450 °C under O_2 flow. The choice of 450 °C was related to the need of attaining sufficient crystallinity without excessively compromising the specific surface area.[21] For electrochemical analysis, the materials (P1 and P2, to give el_1 and el_2 respectively) are deposited onto the conductive support by dropcasting 55 μL of a 3.5 mg/mL dispersion. This corresponds to a loading equal to 1 mg cm^{-2} of Ir. To improve the adhesion of the powder onto the support, 2.5 μL of a 0.15 w% Nafion suspension was added onto the deposit of the iridium oxide nanoparticles.[22] The support is the same used for IrO_x NPs. As reference samples for XAS, $IrCl_3$ (Alfa Aesar) and pure IrO_2 were used. The latter was prepared by calcination at 700 °C under oxygen flux (50 NL/h) for 2 h of $IrCl_3$, which was previously finely ground for 10 min. For XAS measurements, a selected amount of sample was mixed with cellulose and then pressed to a pellet.[23]

2.2. Spectroelectrochemical Cell.[24] It consists of a PTFE cell that contains the electrolyte solution (0.5 M aqueous H_2SO_4), a Pt foil counter electrode, and the reference electrode (AgCl/Ag in 0.1 M KCl). The reference electrode is separated from the solution by a salt bridge consisting of a glass pipet filled with agar containing 0.2 M aqueous $KClO_4$. One side of the cell includes a hole matching with the working electrode area. The working electrode is held between the PTFE cell and a polypropylene plate that also includes a hole for the X-ray beam. All electrochemical and in situ XAS experiments were carried out using a CH Instrument 633D potentiostat, driven by the proprietary software.

2.3. XRPD. High-resolution (HR) and pair distribution function (PDF) quality X-ray powder diffraction (XRPD) measurements on P1 and P2 samples were performed at room temperature at beamlines ID31 and ID15 of the European Synchrotron Radiation Facility (ESRF), respectively. For the two experiments, the same samples were loaded in Kapton capillaries (1.0 mm in diameter) and spun during measurements in order to improve powder randomization.

For HR measurements, data were collected at $\lambda = 0.35420(1)$ Å in the angular range $2° < 2\theta < 48°$ for a total counting time of about 0.5 h/pattern. The wavelength was selected using a

DOI: 10.1021/acscatal.5b01281
ACS Catal. 2015, 5, 5104−5115

double-crystal Si(111) monochromator. The diffracted intensities were detected through nine Si(111) analyzer crystals which spanned over 16° in 2θ. The instrumental resolution function has been determined using Si standard.

For PDF measurements, data were collected at λ = 0.14217(1) Å ($E \approx 87.2$ keV) with a sample detector distance of about 212 mm. Measurements were performed using a MAR 345 Image Plate area detector; for each sample, 15 frames of 6 s were collected. A NIST CeO_2 was used for calibrating the sample to detector distance as well as the instrument-dependent parameters affecting the intensity decay (Q_{damp} = 0.043) and broadening (Q_{broad} = 0.034) of PDF peaks with increasing interatomic distances.

2.4. X-ray Photoelectron Spectroscopy. XPS measurements were performed in an M-Probe Instrument (SSI) equipped with a monochromatic Al Kα source (1486.6 eV) with a spot size of 200 × 750 μm and a pass energy of 25 eV, providing a resolution for 0.74 eV. The energy scale was calibrated with internal reference to the C 1s spectrum of adventitious contamination. The C−C component may be set to a binding energy of 284.6 eV, by default.

With a monochromatic source, an electron flood gun was used to compensate the buildup of positive charge on the insulator samples during the analyses: a value of 10 eV was selected to perform measurements on these samples.

2.5. Transmission Electron Microscopy. TEM images of as-prepared IrO_x nanoparticles (IrO_x_NPs) were acquired using a EF TEM LEO 912AB instrument operated at an accelerating voltage of 120 kV. The TEM grids were prepared by placing a drop of a suspension of NPs on a Formvar-covered copper grid and evaporating the solvent in air at room temperature overnight.

TEM pictures of P1 and P2 were collected with a ZEISS LIBRA200FE energy-filtering transmission electron microscope (EFTEM). All the specimens were suspended in isopropanol and sonicated for 20 min. A drop of the fine suspensions were then dropped onto a holey carbon-coated copper grid and dried overnight.

2.6. XAS. Fluorescence XAS (X-ray absorption spectroscopy) spectra were collected at GILDA beamline (BM-08, European Synchrotron Radiation Facility, ESRF, Grenoble)[25] at the Ir-L_{III} edge. The device employs a 0.8 T Bending Magnet source operating at 6 GeV with typical currents of 200 mA. The characteristics of the beamline are a high resolution ($\Delta E/E \sim 10^{-4}$), a high flux (~10^{11} ph/s), and a few millimeter spot size (typically 1 × 1 mm^2) on the sample. A Si(311) double crystal monochromator was used, the harmonic rejection being realized by Pd mirrors, characterized by a cutoff energy of 20 keV and a 13-element Ge fluorescence detector was employed. The experiments were performed at room temperature, and the spectra were acquired at different potential values: 0.2, 1.0, 1.3, and 1.5 V (quoted versus the reversible hydrogen electrode, RHE). For each potential, three spectra were averaged. This ensures that the material is stable during the spectra acquisitions. The total time involved for the acquisition of spectra, for each potential, is about 6 h.

EXAFS (extended X-ray absorption fine structure) data processing was performed in three steps. The first one consists in the data extraction and was carried out by the use of ATHENA[26] software, belonging to the set of interactive programs IFEFFIT.[27] The second step involves the construction of one or more cluster structures compatible with the structural information known from the literature. Finally, structural parameters were obtained from a fitting procedure (see below). The EXAFS fitting was performed by means of the EXCURVE code.[28] The calculation of the phases and amplitudes is based on the muffin-tin approximation, in the framework of the Hedin−Lundqvist and Von Bart approximations for the exchange and ground state potentials, respectively.[29] This includes the effects of inelastic losses due to the electron inelastic scattering. The fittings were made in the k space, using a k^2 weighting scheme and full multiple scattering calculation within the clusters used in these fits. The goodness of fit (GOF) is given by the F-factor parameter:

$$F = 100 \sum_{N}^{i} \frac{[\chi_{i,\mathrm{exp}} - \chi_{i,\mathrm{calc}}]^2}{\sigma_i} \quad (1)$$

For the XANES (X-ray Absorption Near Edge Structure) analysis, the spectra were first pre-edge subtracted using a straight line, and then normalized to unit absorption coefficient 500 eV above the edge, where the EXAFS oscillations are not visible any more. Further data elaboration is described in more detail in the following.

3. RESULTS AND DISCUSSION

This paragraph describes in depth the morphological and surface composition of P1 and P2 (el_1 and el_2). Due to their preparation procedure, IrO_x_NPs are present as a dispersion in aqueous 1 M NaOH, and it was not possible to perform XRPD and XPS in this media.

3.1. XRPD. *Reciprocal Space Results.* Figure 1a and 1b show the HR-XRPD patterns pertinent to P1 and P2 samples, respectively, along with their Rietveld refinements, while the fitted parameters are reported in Table S1. In the refinements, cell parameters, weight fractions, and an average mean square parameter (U_{mean}) have been allowed to vary as well as background and profile functions.

As to P1, besides an unindexed peak at about 4°, diffraction peaks of NaCl and broad peaks pertinent to metallic Ir are apparent in the pattern, with sharp features (both space group Fm-3m), overlapping with broad bumps (see the green line), suggesting that amorphous phases are also present. In this context, we underline that the weight fractions obtained by the Rietveld refinement and reported in Table S1 refer to the crystalline part of the sample only.

To evaluate the crystallite size (D_V) and the strain (ε) in metallic Ir, Williamson−Hall (WH)[30] analysis of the diffraction peaks of Ir was carried out. The WH plot shows that the Ir phase is constituted by very small ($D_v \approx 3$ nm) and strained ($\varepsilon \approx 0.009$) particles (Figure S1). Moving to P2, the annealing cycle seems to affect deeply the crystalline phase composition, as shown in Figure 1b and Table S1. Broad diffraction peaks related to rutile-like IrO_2 phase ($P4_2/mnm$) appear in the pattern; in P2, IrO_2 is the most abundant crystalline phase (ca. 60%), whereas a significant decrease of the apparent (being calculated only on crystalline phases) Ir and NaCl phase fractions is evident (NaCl lowers to 6%). At the same time, the amount of amorphous phase seems to decrease, at least with respect to the reduction of the background intensity.

As to the microstructure, the peaks of metallic Ir phase sharpen with respect to P1. This is due to both the increase of crystallite dimension ($D_V \approx 7$ nm) and the decrease of strain ($\varepsilon \approx 0.0014$) in this phase. At the same time, the cell parameter a expands with respect to the P1 sample: a = 3.8406(1) Å compared to 3.8365(3) Å. The reduction of cell parameters in

DOI: 10.1021/acscatal.5b01281
ACS Catal. 2015, 5, 5104−5115

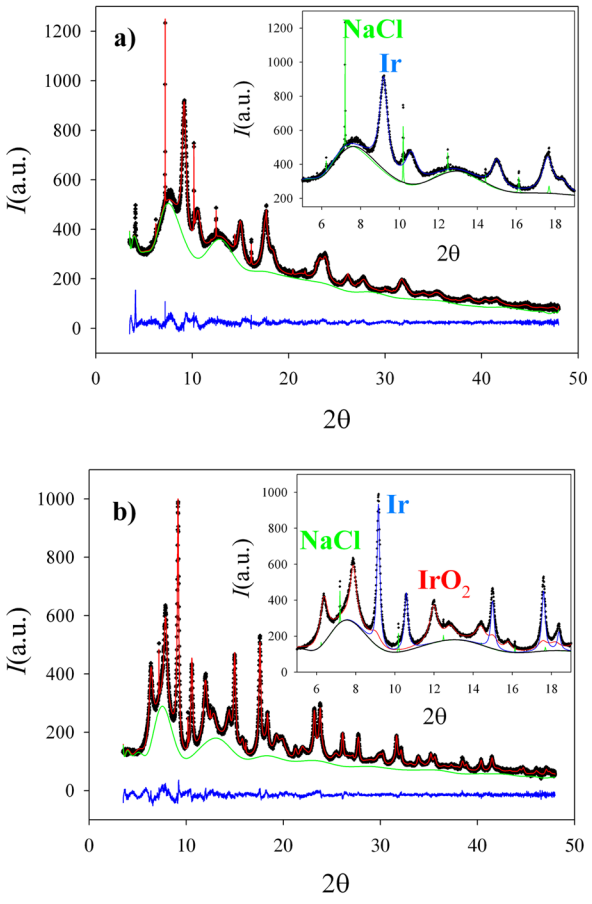

Figure 1. XRPD patterns of P1 (a) and P2 (b) samples. Experimental (black crosses) and calculated (red line) profiles are shown as well as background (green line) and residuals (blue line). The insets highlight the calculated contribution of the Ir (blue line), IrO_2 (red line), and NaCl (green line) phases.

metal nanoparticles is a well-known phenomenon, and it was attributed to the occurrence of tensile stresses at the surface.[31] In addition, crystallite dimension and strain of the IrO_2 phase have been determined using the WH method: $D_V \approx 4$ nm and $\varepsilon \approx 0.006$ (see Figure S1). For a brief discussion of the WH results, see the Supporting Information file.

Real Space Analysis by PDF Quality Diffraction. Figure 2 displays the experimental G(r) curves for P1 and P2 in the range of short interatomic distances; calculated G(r) for Ir and IrO_2 are also shown for reference. The experimental G(r) curves of P1 and P2 in a wider r range are displayed in Figure S2 and have been analyzed using the "Real Space Rietveld" approach.[16,17] Detailed descriptions of the refinement strategies, of the adopted structural models as well as the refined parameters are reported in the Supporting Information.

For both samples, a $G(r)$ peak is present at about 1.55 Å. At very low r values, spurious peaks often appear for several reasons like, e.g., inaccurate background subtraction. However, we should note that the peak position and intensity is quite robust with respect to different data reduction strategies. The nature of this peak will be discussed below.

The experimental G(r) curves of Figure 2 show that Ir and IrO_2 phases are present in both samples; moreover, according to PDF, the most abundant phase is IrO_2 (WF ~ 0.76 for both samples). Conversely, the diffraction peaks of rutile IrO_2 appear only in the pattern of P2 sample (Figure 1). This suggests that

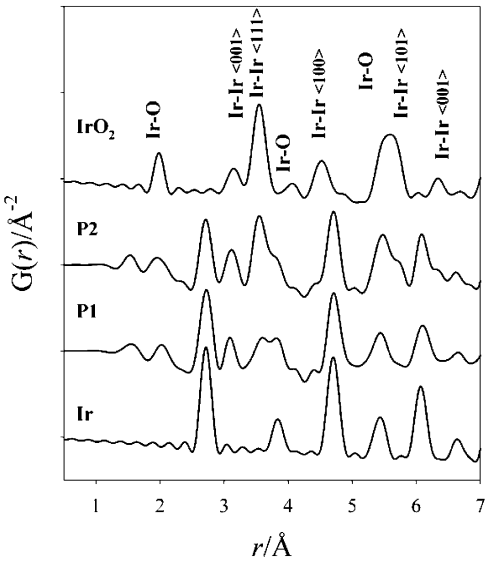

Figure 2. Experimental G(r) curves for P1 and P2 samples at short interatomic distances together with calculated G(r) for Ir and IrO_2. For the IrO_2 phase, the couple of ions which contribute to each G(r) peak and the bond directions in respect to the crystalline axes are also reported.

IrO_2 exists as an amorphous phase in the P1 sample. Accordingly, the determined mean "crystallite dimension" of IrO_2 ($D_V \approx 7$ Å, Table S2) has to be considered as an indication of the extent of short-range order within it.

3.2. XPS. In order to confirm the absence of metallic Ir on the material surface, thus excluding any relevant contribution in the electrochemical response, the surface chemical speciation of Ir was investigated by means of XPS. In particular, the $4f_{7/2,5/2}$ doublet was considered, and the relevant results are reported in Figure 3.

In both materials, XPS reveals the presence of Ir oxides but not of metallic Ir, as the relevant peaks at 60.7 and 63.7 eV[32] are missing. Both spectra present the shape typically observed on IrO_x[33] or IrO_x-based materials,[34,35] with unsymmetrical

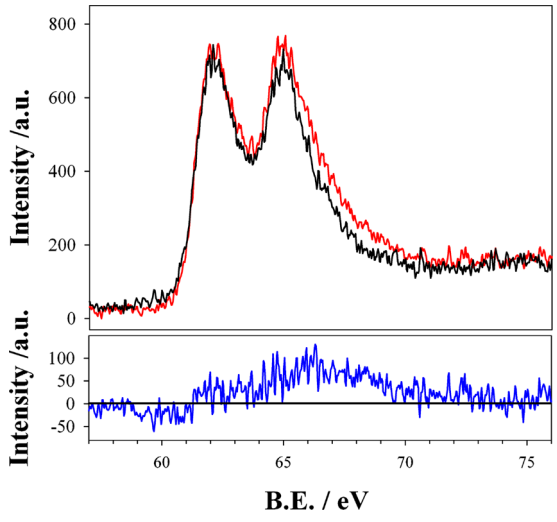

Figure 3. Normalized XPS spectra ($4f_{7/2,5/2}$) of P1 (black line), P2 (red line) and their difference (blue line, bottom box) as a function of binding energy (BE). The intensity of the difference was scaled by a factor of 3 for better readability.

DOI: 10.1021/acscatal.5b01281
ACS Catal. 2015, 5, 5104−5115

peaks, likely due to the copresence of different oxidation states of Ir. The spectra are overlapping: this indicates that the surface composition for the two composites is almost identical. In fact, both peaks ($4f_{7/2}$:62.7 eV and $4f_{5/2}$:65.7 eV) fall very close to the value reported for IrO_2 (with BE for the $4f_{7/2}$ peak ranging from 61.1 to 62.9),[36] thus suggesting the predominance of this speciation, in agreement with both XRD and TEM data (see below). Further peak elaboration for fine surface composition determination is outside the scope of of this work and can easily give rise to artifacts. However, as suggested in ref 33, a direct and fine comparison can be effectively carried out by subtraction. The differential spectra (multiplied by a factor 3 in Figure 3) provide evidence for an increase of spectral weight for the calcined sample (P2) at the highest BE: between 61 eV and 64 for the $4f_{7/2}$ peak and up to 71 eV for the $4f_{5/2}$ peak. This points to a higher average oxidation state of Ir for the calcined sample, likely due to the oxidation of residual Ir(III) from the precursor ($IrCl_3$).

3.3. Morphology by TEM. Figure 4 reports TEM pictures of the synthesized nanoparticles after different synthetic steps.

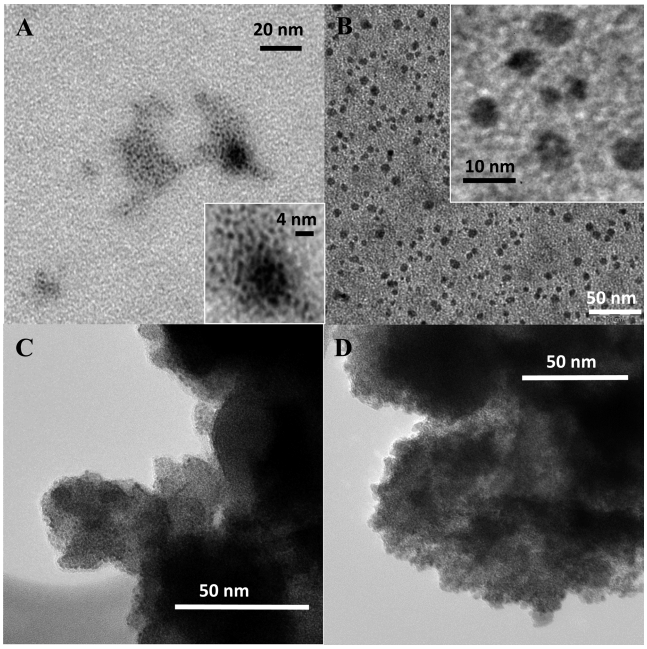

Figure 4. TEM images of (A) as prepared IrO_x nanoparticles; (B) after the dialysis procedure; (C) after drying at 80 °C (that is P1); (D) after calcination (that is P2).

As previously reported,[19] the facile synthesis of IrO_x nanoparticles leads to well-defined and well-dispersed nanoparticles of less than 2 nm in diameter (Figure 4A and inset). After dialysis, but before drying, the nanoparticles agglomerate of about 5−10 nm (Figure 4B and inset).

Interestingly, drying leads to considerable aggregation with formation of a more electron dense, inner component (dark particles in Figure 4C) covered by a less dense "skin", the latter eventually prevailing after calcination (Figure 4D).

In order to elucidate the amorphous/crystalline nature of the particles shown in Figure 4, HR-TEM images have been collected and are shown in Figure 5.

As evident, P1 is rich in crystalline nanoparticles (probably of Ir, because XRD demonstrates that IrO_x is amorphous in this sample, see section 3.1), whereas in sample P2, the whole

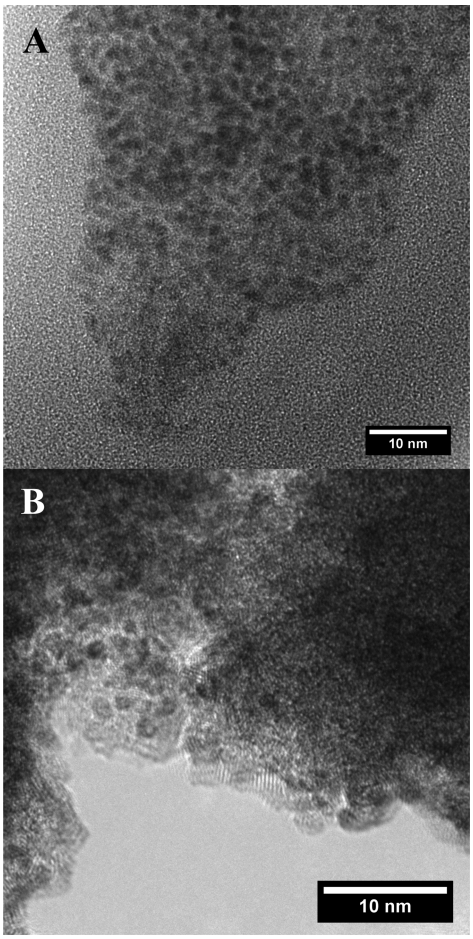

Figure 5. HR-TEM images of P1 (A) and P2 (B).

composite is made of nanocrystals with a high degree of agglomeration, as particularly evident from the crystalline planes evident in the outer shell.

3.4. Electrochemistry. All the applied potential values are quoted versus the reversible hydrogen electrode (RHE).

Cyclic voltammetry of el_1 and el_2 closely resemble the well-known features of IrO_2 that we recently proved by FEXRAV.[24] Figure 6 shows CVs of el_1 and el_2 in comparison with the one recorded on IrO_x_NPs, which is an electrode made of IrO_x nanoparticles[19] (as shown in Figure 4a) before the purification/reduction step.

The CV of all the materials show peaks or bumps relevant to solid-state redox transitions associated with the following generalized equation:

$$IrO_x(OH)_y + \delta H^+ + \delta e^- = IrO_{x-\delta}(OH)_{y+\delta} \quad (1)$$

This corresponds to a transition Ir(III) to Ir(IV) between 0.6 and 1.0 V and from Ir(IV) to Ir(V) for $E > 1.0$ V, as marked with a color bar at the bottom of the figure.[24]

For the sake of a better comparison, in Figure 6 the currents were normalized by the amount of charge Q, obtained by integration of the peak related to the transition Ir(III) → Ir(IV) visible in all curves (between 0.4 and 1.1 V vs RHE at 2 mVs^{-1}).

The behavior of the three materials displays significant differences: (i) el_2 shows the central bumps (Ir (III) to (IV)) only, and the pseudocapacitive characteristics are almost completely covered by double layer capacitance; (ii)

DOI: 10.1021/acscatal.5b01281
ACS Catal. 2015, 5, 5104−5115

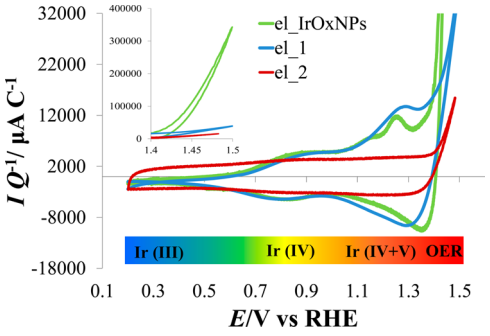

Figure 6. Cyclic voltammograms of el_1(blue line), el_2 (red line) and el_IrO$_x$NPs (green line) in aqueous 0.5 M H_2SO_4. Because of different loadings and for the sake of comparison (el_1 and el_2:1 $mg_{(Ir)}cm^{-2}$; el_IrO$_x$NPs: 0.01 $mg_{(Ir)}cm^{-2}$), currents have been normalized for the voltammetric charge. CVs are recorded at 2 mVs^{-1}. The inset displays the highest I window in the OER region. The color bar at the bottom aims to identifies the Ir speciation prevalent in the potential window of interest, as highlighted in previous works.[11,24]

el_IrO$_x$NPs and el_1 have rather similar CV shapes but the former shows two different peaks for the Ir(IV) → Ir(V) transition. It is possible that the peak at 1.14 V versus RHE for el_2 is masked by the double layer capacitance.

The determination of the number of available sites allows calculating the turnover frequencies (TOF) in dependence on the applied potential starting from steady-state I/E characteristics adopting the following equation:[37]

$$\mathrm{TOF} = \frac{I_{ss}}{n_s n F} \tag{4}$$

where n_s is the number (in moles) of sites (again, determined by integrating the less anodic CV bump), I_{ss} is the corresponding oxygen evolution current (from steady-state I/E curves), and $n = 4$ is the number of electrons per mole of O_2.

The values of TOF obtained from steady-state I/E curve are reported in Figure 7. In all cases, after an initial region at which

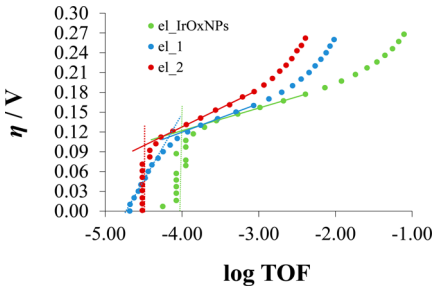

Figure 7. Tafel plot (overpotential versus logarithm of turnover frequency) of the three materials considered in 0.5 M H_2SO_4. Continuous lines represent Tafel lines, whereas dotted lines are meant as extrapolation of the background currents and used for the geometrical estimation of the onset potential.

the material shows no activity (vertical lines until about η = 0.10−0.12 V), straight lines are obtained in a range of 2 orders of magnitude of TOF. At higher TOF values, the slopes of η/log(TOF) lines increase as typically observed for gas evolving catalysts. This has been attributed to either a change of mechanism, or to the change of rate-determining step, or to the saturation of the surface by reaction intermediates or to the blockage of the surface by bubbles. In the present case, the use of a carbon support (needed for in situ XAS, being transparent to X-rays) can also be the result of this slope increase because it is unstable at the highest potentials.

Figure 7 also reports the straight lines corresponding to the Tafel region (dashed lines) as well as lines used for a geometry construction: the intersection of the two is used to estimate the reaction onset potential, E_{OER}.

The values of Tafel line slopes, TOF at 1.4 V and E_{OER} for the three materials are reported in the Table 1.

Table 1. Tafel Line Slope (b), Turnover Frequency at 1.4 V (RHE), and Onset Potential for the Three Materials Herein Considered

	b/mV dec^{-1}	TOF (@1.4 V), s^{-1}	E_{OER}/V
el_IrO$_x$NPs	34.8	4.1×10^{-3}	1.35
el_1	43.3	1.4×10^{-3}	1.34
el_2	56.6	6.2×10^{-4}	1.32

Very interestingly, contrary to previous findings,[38] the Tafel slope b is strongly dependent on the hydration follows the trend el_IrO$_x$NPs < el_1 < el_2 and is likely correlated to the hydration degree of the material. IrO$_x$_NPs represent the most hydrate material, followed by el_1 (treated at 80 °C) and thus by el_2 (treated at 450 °C). Notwithstanding this, the potential for the reaction onset does not change appreciably.

The TOF values were calculated at 1.4 V for the sake of comparison with previous work:[37] in particular, el_1 exhibits the same value obtained for IrO_2 nanoparticles obtained by the sol−gel method: 1.3×10^{-3} s^{-1}.[37]

3.5. EXAFS and XANES. Figure 8 shows Ir-L_{III} edge EXAFS signals of the two samples recorded at 1.0 V (potential value at which almost all iridium is present as Ir(IV), see[24]) and the corresponding Fourier transforms (FT). Oscillations are easily visible above the noise level up to k = 11 $Å^{-1}$. The EXAFS spectrum of an IrO_2 standard sample and the corresponding FT is also shown for reference. IrO_2 is characterized by a well-defined peak at ca. 2 Å, corresponding to the six O neighbors in the rutile structure. The peaks between 3.4 and 3.8 Å are mainly due to Ir and O atoms that are the next-nearest neighbors (NNN) of Ir.

The spectra of the two samples considered in this work are quite different when compared to that of IrO_2. Starting the discussion again from the EXAFS FT, we note that the peak in EXAFS FT situated at distances around 1.8 Å can be attributed to the 2 + 4 oxygen atoms surrounding Ir in a distorted octahedral arrangement. The peak that can be found between 2.8 and 3 Å is due to the presence of an Ir coordination shell, and the peak around 3.5 Å can be explained by the presence of 4 oxygen atoms in the third shell surrounding Ir in iridium oxide.

The peaks at smaller distances (r < 1.8 Å) suggest the presence of heavy atoms as NN (nearest neighbors). In fact, backscattering functions of heavy atoms are characterized by nonmonotonous trends that result in low frequencies in the EXAFS spectra, thus yielding peaks at small distance values in the EXAFS FT.

Accordingly, and on the basis of X-rays diffraction results, the structural model used for the EXAFS fitting is composed of two clusters: one referred to a IrO$_x$ phase and the other to metallic Ir. The energy shift between the origins of the EXAFS of the two clusters, reflecting in turn the different screening of the

DOI: 10.1021/acscatal.5b01281
ACS Catal. 2015, 5, 5104−5115

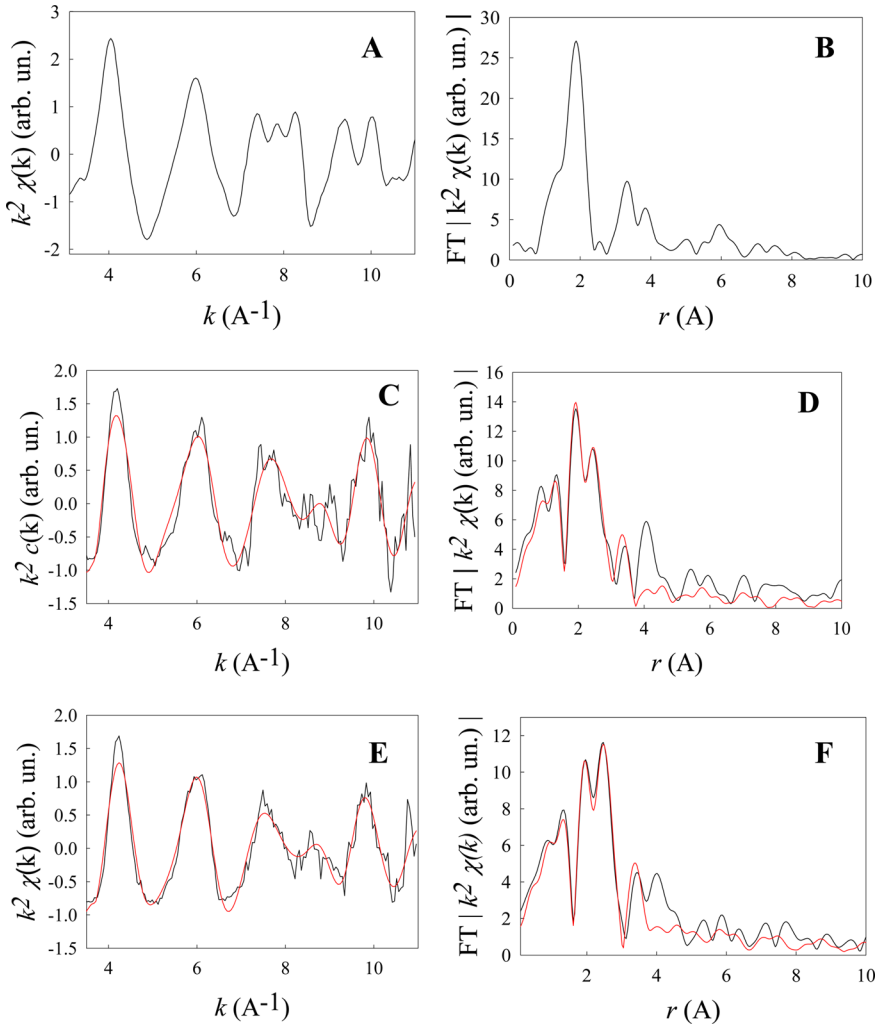

Figure 8. Ir-L_{III} edge EXAFS signals and corresponding FT of IrO_2 (A,B) and of sample (el_1) (C, D) and sample (el_2) (E,F). The experimental signal is the black line, whereas the fit according to the model described in the text is represented by the red line.

Table 2. EXAFS Fitting Parameters for Spectra Shown in Figure 7. ((a): Sample el_1, (b): Sample el_2), *r*: Distances; σ^2: Distance Variances; Coordination Numbers *N* Have Been Kept Constant to Their Crystallographic Values

(a) sample el_1 1.0 V					(b) sample el_2 1.0 V				
cluster 1 IrO_x, multiplicity: 0.75					cluster 1 IrO_x, multiplicity: 0.75				
shell	*N*	atom	*r* (Å)	σ^2 (Å^2)	shell	*N*	atom	*r* (Å)	σ^2 (Å^2)
1	2	O	1.72(6)	4(2) $\times 10^{-2}$	1	2	O	1.72(5)	4(1) $\times 10^{-2}$
2	4	O	1.96(1)	1(1) $\times 10^{-3}$	2	4	O	1.98(1)	3(1) $\times 10^{-3}$
3	2	Ir	2.97(4)	1(4) $\times 10^{-3}$	3	2	Ir	2.8(2)	2(4) $\times 10^{-2}$
4	4	O	3.52(4)	0(5) $\times 10^{-3}$	4	4	O	3.56(2)	0(1) $\times 10^{-3}$
cluster 2 metallic Ir, multiplicity: 0.25					cluster 2 metallic Ir, multiplicity: 0.25				
shell	*N*	atom	*r* (Å)	σ^2 (Å^2)	shell	*N*	atom	*r* (Å)	σ^2 (Å^2)
1	12	Ir	2.63(2)	6(3) $\times 10^{-3}$	1	12	Ir	2.64(1)	4(1) $\times 10^{-3}$
F: 11.1%					*F*: 7.5%				

core electron by the valence electrons, is set at 2 eV. The IrO_x cluster is made up of four coordination shells, whereas the metallic Ir cluster is made up of one shell, as presented in Table 2. The best fit is shown in Figure 8 as red lines, and the final values are reported in Table 2.

Quite interestingly, fitting parameters for the two samples kept at lower (E < 1.0 V) or higher (E > 1.0 V) potential values (1.0 V being the potential at which the concentration of Ir(IV) is at its maximum) are quite similar to each other and do not show any significant difference if compared to results presented above for applied potential equal to 1.0 V (see Supporting Information, Figure S6).

The fittings according to this structural model are also quite good, as supported by the GOF (goodness of fit) *F*, that is around 10% or less for both samples at all the investigated potentials.

In all cases, the IrO_x cluster is characterized by a distorted octahedral geometry because the two apical oxygen atoms are

DOI: 10.1021/acscatal.5b01281
ACS Catal. 2015, 5, 5104−5115

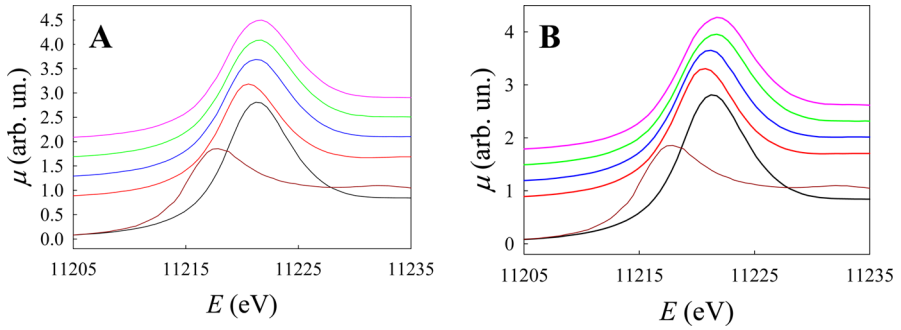

Figure 9. Ir L_{III} edge XANES spectra of el_1 (A) and el_2 (B). Spectra were acquired at 0.2 V (red line), 1.0 V (blue line), 1.3 V (green line), and 1.5 V (pink line). The brown line is the spectrum of metallic Ir, and the black line is the spectrum of bulk IrO_2, shown for reference.

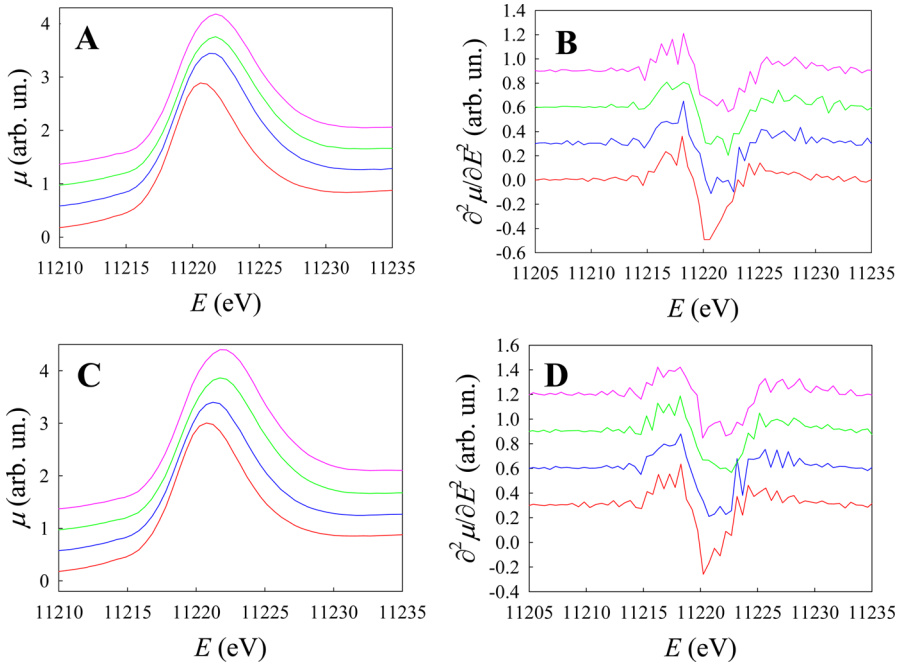

Figure 10. XANES spectra (A,C) and their second derivatives (B,D) of el_1 (A,B) and el_2 (C,D) after the subtraction of metallic iridium contribution. Spectra were acquired at 0.2 V (red line), 1.0 V (blue line), 1.3 V (green line), and 1.5 V (pink line).

situated at a smaller distance if compared to the four equatorial oxygen atoms: this is quite typical of EIROF in acidic environment.[39] In addition, the two short Ir−O bond distance could be at least in part at the origin of the peak in the PDFs found at ca. 1.55 Å. Due to the highly hydrated form of the IrO_x shell, it is quite straightforward to assign the short Ir−O distance to coordination with oxide ions, whereas the long Ir−O distance is assigned to the coordination with OH^- (or H_2O). Indeed, this is similar to that found for 5-fold coordinated Ru in $K_2Ru[O_3(OH)_2]$ with three oxygen atoms at 1.755 Å and 2 OH^- at 2.037 Å[40] or 6-fold coordinated Os in $K_2[OsO_2(OH)_4]$ with two oxygen atoms at 1.77 Å and OH^- at 2.03 Å.[41]

It is also worth pointing out that EXAFS studies on anodic iridium oxide films (AIROF),[42] sputtered iridium oxide films (SIROF)[43] and electrodeposited iridium oxide films (EIROF)[44] reported a decrease of the Ir−O distance (fitted as a single distance) with increasing applied potential. However, in AIROF[42] and EIROF,[44] this is invariably accompanied by a concomitant increase of the corresponding Debye−Waller factor, and/or with very large figures for those parameters, whereas in SIROF, a decrease in the coordination number is observed.[43] It should be noted that in EXAFS the coordination numbers are intrinsically poorly determined as they are strongly correlated with the Debye−Waller factors. In our model, keeping the coordination numbers constant, both the short and long Ir−O distance do not show a sensible variation with the applied potential, and the corresponding Debye−Waller factors do not vary (within the experimental error) and are also quite small (see Supporting Information, Figure S6). This suggests that increasing the applied potential induces in the film local reorganizations by increasing (decreasing) the number of short (long) distances (which is hardly directly visible by EXAFS due to the intrinsic poor sensitivity to coordination numbers, as mentioned above), rather than a simple contraction of the whole coordination IrO_x polyhedra. This possibility to accommodate different bonds with different ligands (oxide and hydroxide ions) at a single Ir site is probably one of the main reasons for which the hosting of Ir in different oxidation states is facile in EIROF[39] and in the present cases.

Finally, we remark that the amount of iridium oxide is larger than metallic Ir and remains almost the same in all the potential range investigated and for both samples.

DOI: 10.1021/acscatal.5b01281
ACS Catal. 2015, 5, 5104−5115

The XANES spectra of the two samples investigated in this work are shown in Figure 9, which reports also those of IrO_2 and metallic Ir for reference.

In the XAS spectrum at the Ir-L_{III} edge, transitions from the 2p to continuum states give rise to a step-like structure, and transitions to localized 5d empty states result in a peak called a white line (WL). The position of the WL can be used for the determination of the oxidation state.[45] At reducing potentials (0.3 V), a shift toward lower energy of the main peak indicates a reduction of Ir, possibly to a state close to Ir(III). As mentioned above, at 1 V, beside the presence of metallic Ir, the position of the main WL indicates that Ir is present mainly as Ir(IV). For more oxidizing conditions, i.e., for 1.3 and 1.5 V, the shift of the main WL toward energies higher than 11221.3 eV and the considerable spectral weight at lower energies indicate the presence of both Ir(III) and Ir(V) species, in agreement with what reported previously on electrodeposited (highly hydrated) iridium oxide films (EIROF).[8]

We can note that the XANES spectra at 1 V can be fitted as linear combinations of the spectra of metallic Ir and IrO_2 (see Figure S7), with weights that are in perfect agreement (25% and 75%, respectively) with those obtained by EXAFS. This suggests that the Ir and the IrO*x* shell are not interacting; therefore, the presence of the metallic Ir core has no relevance on the catalytic mechanisms and can be more effectively discussed starting from difference spectra ($\mu_{(sample)} - \mu_{(metal)} \times 0.25$). Figure 10 shows, after renormalization, these differences, along with their second derivatives. In the second derivatives, the WL gives a negative peak, whereas the step originating from the transitions to continuum states gives almost no contribution, allowing a finer identification of the pertinent oxidation states and electronic structure.[41,42]

It is apparent that, increasing the applied potential, the WL first shifts to increasing energies (from 0.3 to 1 V in the applied potential) and then largely increases in fwhm while shifting toward higher energies (for applied potential larger than 1 V). This is in nice agreement with our previous findings on EIROF,[8] with the remarkable exception that no crystal field splitting is detected at 1.3 V, indicating that in these materials the IrO_6 octahedra are more interacting than in EIROF. Note that a similar effect of hydration on the extension of structural unit interaction was observed by XAS on Ru oxides of different hydration degrees.[46] In the present case, the Ir-metal-subtracted XANES spectra were then fitted by the proper combination of Lorentzian and arctg curves,[47,8] as shown in Figure S7. This allows us to directly assess the Ir oxidation state(s) in both materials as a function of the applied potential.[8,45] The results are shown in Figure 11, demonstrating the presence of both Ir(III) and Ir(V) for $E \geq 1.3$ V.

An alternative way to eliminate the contribution of metallic Ir (provided its passivation by the IrO_x shell) is the determination of $\Delta\mu$, a way often used to characterize the nature of adsorbed species. Concerning the electrochemical applications of XAS, this method was extensively adopted for studying metal nanoparticles used as catalysts in fuel cells.[48]

$\Delta\mu$ spectra, which are reported in Figure 12, are obtained through $\Delta\mu = \mu_E - \mu_{ref,}$ where μ_E and μ_{ref} are the absorption coefficient at the potential of interest and in a reference condition, respectively. In the present case, the reference condition is 1.0 V, i.e. when the presence of Ir(IV) is at its maximum.[24]

In both cases, $\Delta\mu$ shows a dramatic shift of the white line toward lower (0.2 V) or higher (1.3−1.5 V) energies. This in turn indicates that the amount of residual Ir(IV) is relatively low: in particular, the $\Delta\mu$ spectra suggest that the Ir(IV) → Ir (III) transition at 0.2 V is almost complete, while for the Ir(IV) → Ir (V) at 1.3 and 1.5 V, residual Ir(IV) or even Ir(III) cannot be ruled out. At $E = 0.2$ the $\Delta\mu$ spectra are similar for the two samples, whereas at the highest potential values a higher differences are observed for el_2 (Figure 12B).

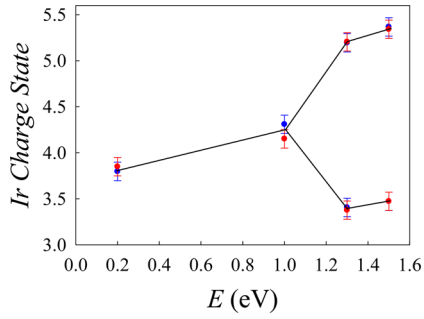

Figure 11. Ir oxidation state values as derived from the fitting of XANES spectra for el_1 (blue dots) and for el_2 (red dots).

4. DISCUSSION

The experimental results shown in section 3 give a clear representation of the IrO_x/Ir particles structure and morphology and the relevant electrochemical features.

XRPD and EXAFS demonstrated the success of the joint purification-and-reduction strategy by evidencing the presence of metallic Ir nanoparticles, while PDF and EXAFS analysis highlighted that IrO_2 and Ir coexist in both samples. Crystalline order in IrO_2 seems to be more extended along the *c* axis than in the ab plane, probably because along the former direction the Ir−O octahedra are edge-sharing. The IrO_2/Ir ratio, which is determined to be ca. 75:25 by both PDF and EXAFS/XANES, is not modified neither by the introduction of the calcination step nor by the application of relatively high potentials.

This interesting result unavoidably leads to the conclusion that Ir particles are included within the IrO_2 shell that acts as protective layer. This was confirmed by XPS. XRPD gives important information on the dimension of IrO_2 and Ir domains: while in the noncalcined sample (P1) IrO_2 exists as an amorphous phase and the Ir phase is made of strained 2.7 nm particles, calcination leads to crystallization of IrO_2 and to an enlargement of the Ir domains.

In P2, XRPD shows the existence of crystalline IrO_2 with domains that have an average diameter of about 4 nm. The crystallization to IrO_2 during the calcinations step is confirmed by XPS that shows an increase of the spectral weight at higher binding energies.

TEM and HRTEM confirm the results suggested by XRD and XPS: in P1, amorphous IrO_x embeds and passivates Ir nanoparticles, whereas after calcination (P2) iridium oxide particles crystallize and masks the metallic core concerning the electron transmission.

For what concerns the electrochemical properties, CVs showed the typical characteristics of hydrous (Ir_NPs and el_1) and low-hydration (el_2) Ir oxide. In all cases, and excluding the portion relevant to OER, the integration of forward and backward scans lead to very similar quantities of charge, meaning that no irreversible processes are present. This is in turn another confirmation of the absence of metallic Ir at the surface: there is no evidence in the existing literature

DOI: 10.1021/acscatal.5b01281
ACS Catal. 2015, 5, 5104−5115

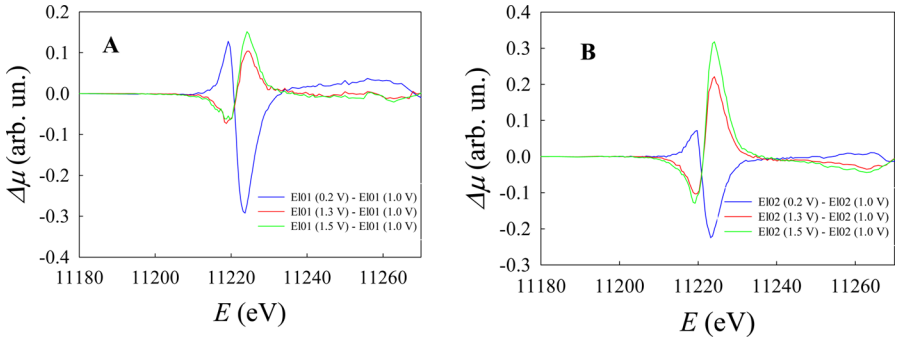

Figure 12. $\Delta\mu$ spectra for el_1 (A) and el_2 (B).

(including the most recent results by FEXRAV)[24] of the reduction of IrO_2 to Ir in the considered potential window.

I/*E* steady-state curves interestingly showed a marked dependency of Tafel line slopes on the material nature and in turn on the hydration degree: Ir_NPs represent amorphous, highly hydrated materials (analogous to electrodeposited iridium oxide films, i.e. with all Ir atoms participating to the electrochemical processes),[49] el_1 also contains amorphous IrO_x (as demonstrated by XRPD) but with a lower degree of hydration having been treated at 80 °C; el_2 underwent a calcination that leads to the lowest hydration.

Here we show that *b*, the Tafel slope, follows the trend Ir_NP < el_1 < el_2 meaning that the hydrated nanoparticles have a higher intrinsic activity. This is likely bound to the observation of Kim et al.[50] that the pH sensitivity is higher (higher mV/pH slopes) for hydrous IrO_x than for thermally treated films. We can suggest that the amount of water trapped within the catalyst has a positive influence on the reaction mechanism, likely enhancing the formation of vicinal Ir(V) sites, and this can be directly related either to the hydration itself or to the higher mobility and defectivity of Ir centers (or both).

In parallel, losing hydration means reducing the percentage of electrochemically active Ir centers. It has been proved by us[51] and by Fierro et al.[52] that for heat-treated (high crystallinity-low hydration) IrO_2 particles, only 1−2% of Ir atoms participates to the electrochemical phenomena, whereas for hydrous IrO_x layers, the percentage is very close to 100%.[51]

As mentioned, this low surface-to-bulk ratio of X-ray absorbers hindrances any electrochemical XAS studies on low hydration oxides. We stepped over this issue by the herein described synthetic strategy of including a nonoxidized Ir core, which allowed us to observe the presence of more than one oxidation state, likely Ir(III) and Ir(V), after subtracting the contribution of metallic Ir from the XANES spectra for applied potentials ≥1.3 V.

This result explains why the onset potential E_{OER} of materials with different hydration are rather similar and in good agreement with our previous results on EIROF,[11,24] with the warning that for the EIROF material at 1.3 V, a single oxidation state was detected (Ir(IV)), together with crystal field splitting for the 5*d* states.[11,24] This can occur only when the IrO_6 octahedra are noninteracting,[53,54] a condition bound to the hydrous/amorphous nature of EIROF. In the present case, XRPD results imply a strong connectivity for sample P2 of the IrO_6 octahedra, at least along the *c* axis. As PDF and EXAFS outcomes for samples P1 and P2 (el_1 and el_2) are very similar, it is safely assumed that the conclusion of a strong connectivity also holds for sample P1 (el_1). This high connectivity may switch on the interaction between the IrO_6 octahedra, thus allowing band formation and preventing crystal field splitting to be evident. The interaction among octahedra and its dependence on the oxide hydration degree was previously observed in Ru oxides[46] and has a key role in the material behavior, since hydration (and thus ion mobility through the layer) and octahedra interaction (giving rise to electronic conductivity) have a counterbalanced effect in the final transport of species participating to pseudocapacitive phenomena and to the OER.

However, the choice between good ionic or electronic conductivity can be adjusted by a correct material design: nanoparticles might promote both a high surface area (number of active sites) exposed to the electrolyte and a good interaction between the octahedra, the latter leading to the formation of electron energy bands and thus improving electric conductivity. el_1 and el_2 respond to this demand, as well demonstrated by the fact that any potential change leads to redox activity of the large majority of Ir sites (Figure 12) thanks to the small dimension of the Ir−O domains. This in turn allowed observing the oxidation states assumed by Ir at the different applied potential, showing a net prevalence of Ir(III) at 0.2 V and of Ir(V) at 1.3 and 1.5. In addition, a closer inspection of the white lines for E = 1.3 and 1.5 V evidenced the presence of two oxidation states, as highlighted for EIROF[11] likely bound to the existence of different speciation of Ir in the OER catalytic cycle. However, this view requires review in the framework of materials that possess interacting octahedra and that can be hardly drawn as a molecular-like catalyst. Octahedra interaction makes then the electrons and holes formed at 1.3 V itinerant (quasi-free); they can be detected by XANES just thanks to the very fast (ca. 10^{-12} s) time scale of the technique. Increasing the potential to 1.5 V allows the formation of more Ir(V): now Ir(V) can be present on vicinal sites at the surface, thus starting the catalytic circle as proposed by Steegstra et al.[55]

In operando EXAFS also demonstrates that the IrO_x cluster parameters do not change under the application of increasing potentials, and this includes those at which oxygen evolution occurs. This important result, which was recently partially shown also in the case of time-resolved experiments of hydrous IrOx,[39] suggests that the IrO cluster can accommodate different oxidation states without an appreciable change of the structural parameters. This in turn suggests that a small reorganization energy exists for the IrO cluster during OER, a prerequisite for the well-known high activity of IrO_2.

It has to be highlighted that the same set of data provided (i) the evidence of the participation of iridium in the catalytic cycle of water oxidation and (ii) the connection between the high turnover frequency and the low reorganization effort for the

DOI: 10.1021/acscatal.5b01281
ACS Catal. 2015, 5, 5104−5115

catalytic site to accommodate the state of charge that has to be assumed to complete the cycle.

3. CONCLUSIONS

In this work, three IrO_2-based materials with different hydration degree have been compared in terms of electrocatalytic activity toward the oxygen evolution reaction (OER).

The synthesis of Ir/IrO_2 powders was carried out with a single-step reduction + purification procedure to attain a high surface/bulk ratio of Ir−O centers, allowing us to carry out in operando XAS experiments.

Electrochemical characterization has been performed in parallel to morphological and structural (XRD, also with PDF and TEM) and surface (XPS) analyses.

PDF and EXAFS analysis highlighted that IrO_2 and Ir nanoparticles coexist in both samples. The IrO_2/Ir ratio (ca. 75:25) is not modified neither by the introduction of the calcination step nor, in situ, by application of relatively high potentials.

This was confirmed by TEM images that demonstrate the effectiveness of the adopted synthetic method: the Ir particles are passivated by the IrO_x layer present around them.

Very interestingly, only the Ir−O shell (and not the metallic Ir core) is sensitive to the applied potential. This allowed us to carry out in operando XAS experiments, which confirmed the Ir(III)−Ir(V) catalytic cycle previously observed on hydrous IrO_x. This represents a breakthrough, because it extends the mechanism proposed earlier by us to high-stability materials, such as those adopted at the industrial level.

Notwithstanding the similarity of hydrous/nonhydrous materials in terms of general mechanism, the Tafel slope decreases with increasing hydration degree. This can be ascribed to either a higher ability of hydrous materials in generating active (vicinal) Ir(V) centers or to an improved proton mobility.

In addition to the observation of the catalytic cycle, which represents by itself an important outcome, we observe that the morphology of IrO_2 clusters does not change appreciably under OER conditions. This can be at the basis of low reorganization energies that in turn might be at the basis of the well-known activity of IrO_2.

■ ASSOCIATED CONTENT

Supporting Information

The Supporting Information is available free of charge on the ACS Publications website at DOI: 10.1021/acscatal.5b01281.

Rietveld refinement and Williamson−Hall analysis on XRPD patterns of samples P1 and P2; Williamson−Hall plots for metallic Ir phases in P1, P2 samples and for IrO_2 phase in P2 sample; real space Rietveld analysis of the PDF data pertinent to P1 and P2 samples; interatomic distances for the first and the second coordination shells of oxygen atoms for el_1 and el_2 and their Debye−Waller Factors for el_1 and el_2 (PDF)

■ AUTHOR INFORMATION

Corresponding Author

*E-mail: alessandro.minguzzi@unimi.it.

Notes

The authors declare no competing financial interest.

■ ACKNOWLEDGMENTS

The authors gratefully acknowledge Ministero dell'Istruzione, dell'Università e della Ricerca (MIUR) for funding (Futuro in Ricerca 2013, project RBFR13XLJ9) and the European Synchrotron Radiation Facility for provision of beam time at BM 08 (LISA) and ID31 beamlines. C.L. is grateful to Università degli Studi di Milano for her postdoctoral fellowship. O.L. is grateful to Università degli Studi di Milano and MIUR for his PhD and postdoctoral fellowships, respectively. We are grateful to Istituto di Scienze e Tecnologie Molecolari (ISTM-CNR) and CIMA (Centro Interdipartimentale di Microscopia Avanzata) for their support in collecting TEM and HRTEM images.

■ REFERENCES

(1) Trasatti, S. *Electrochim. Acta* **1984**, *29*, 1503−1512.
(2) Minguzzi, A.; Locatelli, C.; Cappelletti, G.; Bianchi, C. L.; Vertova, A.; Ardizzone, S.; Rondinini, S. *J. Mater. Chem.* **2012**, *22*, 8896−8902.
(3) Antolini, E. *ACS Catal.* **2014**, *4*, 1426−1440.
(4) Oh, H.-S.; Nong, H. N.; Reier, T.; Gliech, M.; Strasser, P. *Chem. Sci.* **2015**, *6*, 3321−3328.
(5) Xu, J.; Aili, D.; Li, Q.; Christensen, E.; Jensen, J. O.; Zhang, W.; Hansen, M. K.; Liu, G.; Wang, X.; Bjerrum, N. J. *Energy Environ. Sci.* **2014**, *7*, 820−830.
(6) Sivula, K.; Le Formal, F.; Grätzel, M. *ChemSusChem* **2011**, *4*, 432−449.
(7) Ye, H.; Park, H. S.; Bard, A. J. *J. Phys. Chem. C* **2011**, *115*, 12464−12470.
(8) Marelli, M.; Naldoni, A.; Minguzzi, A.; Allieta, M.; Virgili, T.; Scavia, G.; Recchia, S.; Psaro, R.; Dal Santo, V. *ACS Appl. Mater. Interfaces* **2014**, *6*, 11997−12004.
(9) Minguzzi, A.; Fan, F-R F.; Vertova, A.; Rondinini, S.; Bard, A. J. *Chem. Sci.* **2012**, *3*, 217−229.
(10) Morozov, A.; De Battisti, A.; Ferro, S.; Martelli, G. N. International Patent WO 2005/014885 A1.
(11) Minguzzi, A.; Lugaresi, O.; Achilli, E.; Locatelli, C.; Vertova, A.; Ghigna, P.; Rondinini, S. *Chem. Sci.* **2014**, *5*, 3591−3597.
(12) Smith, R. D. L.; Prévot, M. S.; Fagan, R. D.; Zhang, Z.; Sedach, P. A.; Siu, M. K. J.; Trudel, S.; Berlinguette, C. P. *Science* **2013**, *340*, 60−63.
(13) Danilovic, N.; Subbaraman, R.; Chul Chang, K.-C.; Chang, S. H.; Kang, Y. J.; Snyder, J.; Paulikas, A. P.; Strmcnik, D.; Kim, Y.-T.; Myers, D.; Stamenkovic, V. R.; Markovic, N. *J. Phys. Chem. Lett.* **2014**, *5*, 2474−2478.
(14) Lin, F.; Boettcher, S. W. *Nat. Mater.* **2014**, *13*, 81−86.
(15) Egami, T.; Billinge, S. J. L. In *Underneath the Bragg Peaks: Structural Analysis of Complex Materials*, Vol. 7; Cahn, R. W., Ed.; Pergamon Press: Oxford, 2003.
(16) Scavini, M.; Coduri, M.; Allieta, M.; Brunelli, M.; Ferrero, C. *Chem. Mater.* **2012**, *24*, 1338−1345.
(17) Coduri, M.; Scavini, M.; Brunelli, M.; Allieta, M.; Ferrero, C. *Chem. Mater.* **2013**, *25*, 4278−4289.
(18) Nakagawa, T.; Beasley, C. A.; Murray, R. W. *J. Phys. Chem. C* **2009**, *113*, 12958−12961.
(19) Nakagawa, T.; Bjorge, N. S.; Murray, R. W. *J. Am. Chem. Soc.* **2009**, *131*, 15578−15579.
(20) Díaz-Álvarez, A. E.; Cadierno, V. *Appl. Sci.* **2013**, *3*, 55−69.
(21) Marshall, A.; Tsypkin, M.; Børresen, B.; Hagen, G.; Tunold, R. *J. New. Mater. Electrochem. Systems* **2004**, *7*, 197−204.
(22) Locatelli, C.; Minguzzi, A.; Vertova, A.; Rondinini, S. *J. Appl. Electrochem.* **2013**, *43*, 171−179.
(23) Minguzzi, A.; Locatelli, C.; Cappelletti, G.; Scavini, M.; Vertova, A.; Ghigna, P.; Rondinini, S. J. *J. Phys. Chem. A* **2012**, *116*, 6497−6504.
(24) Minguzzi, A.; Lugaresi, O.; Locatelli, C.; Rondinini, S.; D'Acapito, F.; Achilli, E.; Ghigna, P. *Anal. Chem.* **2013**, *85*, 7009−7013.

DOI: 10.1021/acscatal.5b01281
ACS Catal. 2015, 5, 5104−5115

(25) D'Acapito, F.; Colonna, S.; Pascarelli, S.; Antonioli, G.; Balerna, A.; Bazzini, A.; Boscherini, F.; Campolungo, F.; Chini, G.; Dalba, G.; Davoli, I.; Fornasini, P.; Graziola, R.; Lichieri, G.; Meneghini, C.; Rocca, F.; Sangiorgio, L.; Sciarra, V.; Tullio, V.; Mobilio, S. *ESRF Newsletter* **1998**, *30*, 42−44.
(26) Ravel, B.; Newville, M. *J. Synchrotron Radiat.* **2005**, *12*, 537−541.
(27) Newille, M. *J. Synchrotron Radiat.* **2001**, *8*, 322−324.
(28) Binsted, N.; Hasnain, S. S. *J. Synchrotron Radiat.* **1996**, *3*, 185−196.
(29) Gurman, S. J.; Binsted, N.; Ross, I. *J. Phys. C: Solid State Phys.* **1984**, *17*, 143−152.
(30) Williamson, G. K.; Hall, W. H. *Acta Metall.* **1953**, *1*, 22−31.
(31) Diehm, P. M.; Ágoston, P.; Albe, K. *ChemPhysChem* **2012**, *13*, 2443−2454.
(32) Moulder, J. F.; Stickle, W. F.; Bomben, K. D. In *Handbook of X-ray Photoelectron Spectroscopy*; Perkin Elmer: Eden Praie, MN, 1992.
(33) Sanchez Casalongue, H. G.; Ng, M. L.; Kaya, S.; Friebel, D.; Ogasawara, H.; Nilsson, A. *Angew. Chem., Int. Ed.* **2014**, *53*, 7169−7172.
(34) Ardizzone, S.; Bianchi, C. L.; Cappelletti, G.; Ionita, M.; Minguzzi, A.; Rondinini, S.; Vertova, A. *J. Electroanal. Chem.* **2006**, *589*, 160−166.
(35) Ardizzone, S.; Bianchi, C. L.; Borgese, L.; Cappelletti, G.; Locatelli, C.; Minguzzi, A.; Rondinini, S.; Vertova, A.; Ricci, P. C.; Cannas, C.; Musinu, A. *J. Appl. Electrochem.* **2009**, *39*, 2093−2105.
(36) NIST Technology Services. http://srdata.nist.gov (accessed, May 2015).
(37) Locatelli, C.; Minguzzi, A.; Vertova, A.; Cava, P.; Rondinini, S. *Anal. Chem.* **2011**, *83*, 2819−2823.
(38) Fierro, S.; Kapałka, A.; Comninellis, C. *Electrochem. Commun.* **2010**, *12*, 172−174.
(39) Achilli, E.; Minguzzi, A.; Lugaresi, O.; Locatelli, C.; Rondinini, S.; Spinolo, G.; Ghigna, P. *J. Spectrosc.* **2014**, *2014*, Article no. 480102.
(40) Fischer, D.; Hoppe, R. *Z. Anorg. Allg. Chem.* **1991**, *601*, 41−46.
(41) Atovmjan, O.; Andjanov, V. G.; Poraj-Kosic, M. A. *J. Struct. Chem.* **1962**, *3*, 660−664.
(42) Hüppauff, M.; Legender, B. *J. Electrochem. Soc.* **1993**, *140*, 598−602.
(43) Pauportè, T.; Aberdam, D.; Hazemann, J.-L.; Faure, R.; Durand, R. *J. Electroanal. Chem.* **1999**, *465*, 88−95.
(44) Mo, Y.; Stefan, I. C.; Cai, W.-B.; Dong, J.; Carey, P.; Scherson, D. A. *J. Phys. Chem. B* **2002**, *106*, 3681−3686.
(45) Hillman, A. R.; Skopek, M. A.; Gurman, S. *Phys. Chem. Chem. Phys.* **2011**, *13*, 5252−5263.
(46) McKeown, D. A.; Hagans, P. L.; Carette, L. P. L.; Russell, A. E.; Swider, K. E.; Rolison, D. R. J. *J. Phys. Chem. B* **1999**, *103*, 4825−4832.
(47) Ghigna, P.; Spinolo, G.; Scavini, M.; Tamburini, U. A.; Chadwick, A. V. *Phys. C* **1995**, *253*, 147−155.
(48) Ramaker, D. E.; Koningsberger, D. C. *Phys. Chem. Chem. Phys.* **2010**, *12*, 5514−5534.
(49) Petit, M. A.; Plichon, V. *J. Electroanal. Chem.* **1998**, *444*, 247−252.
(50) Kim, T. Y.; Yang, S. *Sens. Actuators, B* **2014**, *196*, 31−38.
(51) Minguzzi, A.; Locatelli, C.; Cappelletti, G.; Bianchi, C. L.; Vertova, A.; Ardizzone, S.; Rondinini, S. *J. Mater. Chem.* **2012**, *22*, 8896−8902.
(52) Fierro, S.; Nagel, T.; Baltruschat, H.; Comninellis, C. *Electrochem. Commun.* **2007**, *9*, 1969−1974.
(53) Choy, J.-H.; Kim, D.-K.; Hwang, S.-H.; Demazeau, G.; Jung, D.-Y. *J. Am. Chem. Soc.* **1995**, *117*, 8557−8566.
(54) Choy, J.-H.; Kim, D. K.; Demazeau, G.; Jung, D.-Y. *J. Phys. Chem.* **1994**, *98*, 6258−6262.
(55) Steegstra, P.; Busch, M.; Panas, I.; Ahlberg, E. *J. Phys. Chem. C* **2013**, *117*, 20975−20981.

DOI: 10.1021/acscatal.5b01281
ACS Catal. 2015, 5, 5104−5115